International Journal of Rock Mechanics & Mining Sciences 79 (2015) 55–62

Contents lists available at ScienceDirect

International Journal of Rock Mechanics & Mining Sciences

journal homepage: www.elsevier.com/locate/ijrmms

Integrated measurements of permeability, effective porosity, and specific storage of core samples using water as the pore fluid

Jianye Chen [a,b,*], Xiaosong Yang [a], Qingbao Duan [a], Colin Peach [b]

[a] State Key Laboratory of Earthquake Dynamics, Institute of Geology, China Earthquake Administration, Beijing, China
[b] HPT Laboratory, Department of Earth Sciences, Utrecht University, Utrecht, Netherlands

ARTICLE INFO

Article history:
Received 26 January 2015
Received in revised form
19 July 2015
Accepted 8 August 2015

Keywords:
Integrated measurements of transport properties
Pore pressure oscillation technique
Microvolumeter
Permeability–porosity–storativity

1. Introduction

Permeability (k), effective porosity (Φ), and specific storages (S_s) are the parameters which are often concerned when evaluating the transport properties of porous rocks. Ideally, the intrinsic transport properties of the rocks do not depend on the type of pore fluid; therefore both gas and liquid can be used as the pore fluid for the laboratory measurements, although the Klinkenberg effect on gas permeability needs to be corrected. Due to the high chemical stability and high performance convenience,[1,2] gas has been favored by most rock-physicists.[3,4] In addition, the compressibility and viscosity of gas are less sensitive to temperature variations than those of water, so the measurement error due to these factors is less likely to be introduced. When gas is the pore fluid, permeability can be measured by the steady-state or a transient method such as a pulse-decay and pore pressure oscillation technique,[5,6] and porosity by the gas expansion method, based on the Boyle–Mariotte equation for an isothermal gas.[7,8] By properly arranging the procedure of the measurement, permeability and porosity of a dry sample can be measured concurrently in a single experiment.[9]

Under most natural conditions at the upper crustal depth, rocks are expected to be water-saturated, so the gas properties are unlikely to be directly relevant except in some circumstances such as in the gas fields. Previous studies have shown that permeability of a sample to gas is higher (up to 1.8 orders of magnitude) than the permeability of the same sample to water, even after correction for the Klinkenberg effect.[9–13] For some rock types like shale, strong physicochemical interactions may occur between the skeletal grains and the aqueous pore fluid,[2,11] which influences the flow characteristics of these rocks.[14] Against this background, it is important to determine the transport properties of porous rocks under water conditions. However, in laboratories liquid was seldom used as the pore medium for the concurrent measurement of these parameters.[15–18] The most significant difficulty lies in the measurement of porosity. The current standard techniques for porosity measurement (mercury intrusion porosimetry, 2-D image analysis, CT, NMR imaging, and dry vs. wet weighing) cannot be readily applied under high confining pressure. The use of a high-precision volumetric pump allows for the quantification of the pore volume change in response to the change in confining pressure,[15,19] but it cannot tell the absolute, effective porosity of the sample.[16] To solve this problem, some measured the initial water porosity at atmospheric pressure by means of a standard method stated above.[16,20–23] Alternatively, some measured the gas porosity of a dry sample at an initial pressure and then transferred to water condition at the same pressure.[8] However, these strategies encounter problems if incohesive rocks such as fault rocks are involved, or the sample measured contains swelling mineral(s) or

* Corresponding author at: Institute of Geology, China Earthquake Administration, Qijiahuozi, P.O. BOX 9802, Beijing 100029, China. Fax: +86 10 62009030.
E-mail address: jychen@ies.ac.cn (J. Chen).

http://dx.doi.org/10.1016/j.ijrmms.2015.08.007
1365-1609/

generally contains abundant phyllosilicates. Adsorption of water can cause clay clusters to expand in size, even in the absence of swelling clays, and reduce the pore space.[24,25] Delamination and migration of particles, which then block the small pore throats, is also possible in the presence of abundant phyllosilicates,[12,26] because the clay minerals usually have lower frictional strength when wet than dry,[27] thus facilitating reorientation of particles during compaction. Taken together, it is important to develop a method for determination of the absolute porosity under in-situ hydrological conditions.

Recently, a fluid-flow apparatus was developed at the Institute of Geology, China Earthquake Administration. By employing several techniques, this system allows for the integrated measurements of permeability, effective porosity, and specific storage, under elevated confining pressures.

2. Experimental method and procedure

As a conventional fluid-flow apparatus, the system consists of a pressure vessel, along with the standard units for controlling confining and pore pressures, as shown in Fig. 1.[8] With an intensifier, the confining pressure can reach a maximum of 200 MPa, with fluctuations varying within 0.3 MPa. A maximum fluid pressure of 40 MPa can be used for the steady-state flow method, and a maximum mean value of ~36 MPa for the oscillatory fluid pressures when using the transient method. To maintain constant temperature in and around the sample, the pressure vessel, along with the connecting tubing, valves and fittings that are crucial for the measurement, are enclosed in a polystyrene-foam chamber in size of ~1 m^3 (see the box in Fig. 1). The temperature probe used (Fluke 1523) has a resolution of 1 mK. Using a digital temperature controller, lamp heater and fan (Fig. 1), the temperature within the chamber can be controlled at a desired value (25–30 °C), with fluctuations less than 0.1 K throughout an experiment. In the measurement, by choosing different "fluid reservoirs", either gas or liquid can be used as the pore fluid (Fig. 1). Independent pipelines are used when the gas and liquid work as pore fluids. In the present study, only liquids were employed.

2.1. Method for individual parameters

2.1.1. Permeability (k)

The versatile measurements of permeability were enabled by employing two syringe pumps ("P_f self-controlled unit"), as illustrated in Fig. 1, which can provide a constant flow (5–40,000 μL/min) and a sinusoidal oscillating pressure (20 s < period < 2400 s). In regards to the steady-state flow method, the flow rate was determined by a balance or a high-precision flowmeter (Fig. 1). The pore pressure oscillation (PPO) method has been well described in previous publications.[28,29] Therefore, only a brief description is given here. A pressure signal of the sinusoidal oscillation was imposed at the upstream end of the sample, and the response at the downstream end was recorded (Fig. 2a). A Fourier analysis was performed on the two signals to obtain the amplitude ratio ($0<\alpha<1$) and phase delay ($\theta<0$). From these two measured parameters, two dimensionless parameters were calculated using a numerical analysis based on the equations given by Fischer and Paterson,[6] from which the permeability (k) and specific storage (S_s) of the sample were calculated. The relative uncertainties for k and S_s were further determined following the method given by Bernabé et al.[29]

The storage of the downstream reservoir (B_d) is the most important parameter for the PPO method, and in previous studies was either calibrated by subtracting the upstream storage from the storage of the entire system,[6] or calculated through multiplying the system volume by fluid compressibility.[5] Our verification tests indicated that these methods could introduce relatively large errors in B_d, and thus in the measurement results, particularly for S_s. In our system, B_d was directly measured using a specifically designated microvolumeter, which basically consisted of a valve and a LVDT (Fig. 1). The variable B_d could be achieved (if needed) by

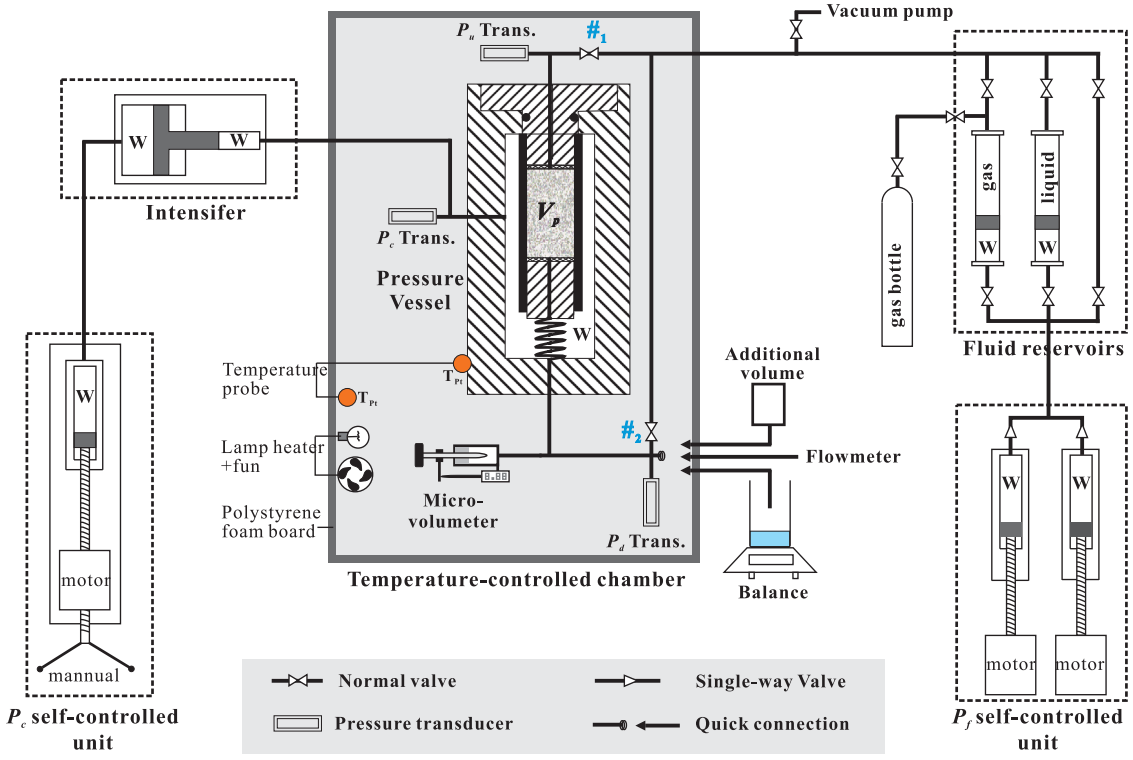

Fig. 1. Diagram showing the fluid-flow system for integrated transport property measurements.

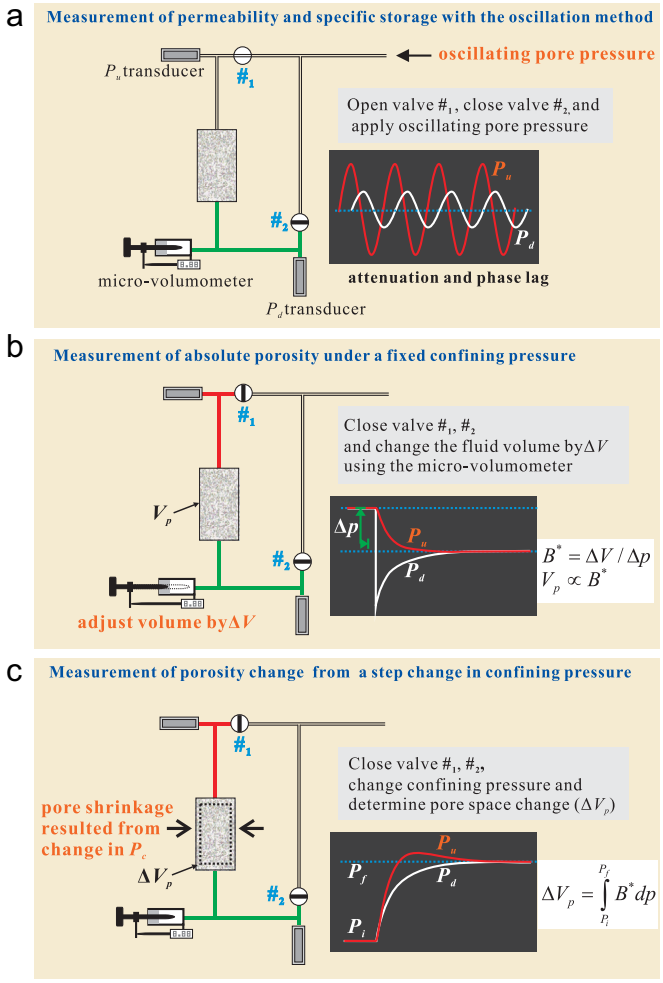

Fig. 2. Diagram showing the methods for measuring: (a) permeability, specific storage; (b) absolute porosity; and (c) relative porosity change.

changing the "additional volume" (Fig. 1).

2.1.2. Effective porosity (Φ)

The effective porosity of a sample is obtained by measuring the absolute porosity at an initial (reference) pressure, and the porosity changes in response to different pressure steps. The absolute porosity is determined using a microvolumeter. As shown in Fig. 2b, in this measurement, valves #1 and #2 were closed in order to isolate a closed fluid system, which consisted of the testing sample plus the upstream and downstream pipes. By slightly withdrawing the microvolumeter, the downstream pressure immediately decreased. Following the equilibrium, the upstream and downstream pressures merged together. The storage of the enclosed system was calculated as $B^* = \Delta V/\Delta p$, where ΔV is the volume change imposed by the microvolumeter, and Δp is the resultant pressure change. The pore volume of the sample (V_p) could then be interpolated from a database of B^* versus V_p, and calibrated in advance as detailed below.

The calibration was performed using a series of hard-alloy cylinders, containing holes of various diameters. For each cylinder, the system storage was determined (B^*) at a range of pressures (Fig. 3a). From this dataset, the B^*-value for any pore volume (V_p) at any pressure within the range investigated could be interpolated. As shown in Fig. 3b, the system storage against pore volume is presented at selected pressures. The results exhibit clear linear relations for all the pore volumes used in the calibration, and show slightly decreasing slopes with the increase of pressure. These slopes (4.57×10^{-10}–4.01×10^{-10} Pa^{-1}) were exactly consistent with the compressibility of pure water in the experimental conditions of our measurements (4.55×10^{-10}–4.06×10^{-10} Pa^{-1} at room temperature and 15–35 MPa, http://webbook.nist.gov/chemistry/fluid/), which testified to the high confidence of the calibration. On this basis, it was believed that the storage of the enclosed system (B^*) essentially consisted of two components. These were the storage of the sample (B), which is proportional to the pore volume (V_p) with fluid compressibility (β_f) as the proportionality factor, and also the storage of the pipes (B_{pipe}) which, as indicated by the intercepts, varied with the fluid pressure (Fig. 3b inset). At a given fluid pressure, this relation can be expressed as follows:

$$B^* = B_{pipe} + B_f V_p \tag{1}$$

This relation is the basis for the absolute porosity measurement. In accordance with the calibration data and provided a typical core sample with a diameter of 20 mm and a length of 10 mm ($\varphi 20 \times 10$ mm^2), our method for measuring absolute porosity was found to be theoretically valid for porosities in the range of 0.5–32% (Fig. 3b).

Porosity changes in response to a change in P_c, and is evaluated from the pore pressure change.[8] In the measurement, valves #1 and #2 were again closed to obtain a closed system (Fig. 2c). The confining pressure was then stepped upward or downward, resulting in a shrinkage or swelling of the sample and thus fluid pressurization or depressurization from P_i to P_f (Fig. 2c). Due to the different pipe volumes, the pressure changes at the two ends of the sample were different. However, they were believed to merge together with time. The pore volume change (ΔV_p) could be calculated by integrating B^* over the pressure change, i.e., $\Delta V_p = \int_{P_i}^{P_f} B^* dp$. Having obtained the pore volume change, the pore volume (V_p) and effective porosity (Φ) of the sample at each P_c step could be evaluated as "$V_{p0} + \sum \Delta V_p$" and "$V_p/(V_p + V_m)$", respectively, where V_{p0} is the initial (reference) pore volume determined using the method described above, and V_m is the grain volume, which was measured initially with a gas pycnometer, and then corrected to high pressures using grain compressibility of the sample[30] (Table 1).

2.1.3. Specific storage (S_s)

Specific storage is defined as the volume change of the pore fluid contained in a unit-volume sample due to a unit fluid pressure change. In this study's measurement, there were two ways for determining the specific storage. First of all, the specific storage could be gained simultaneously with the permeability by using the PPO method (termed as S_s-I). It has been addressed in previous research results that the S_s-I data might suffer uncertainties,[29] and the principal reason lies on the fact that the measuring systems usually have a much larger downstream storage than the rock samples themselves. By assuming a core sample in size of $\varphi 20 \times 10$ mm^2 that has a typical S_s-value of 1×10^{-10} Pa^{-1},[31] then the storage of this sample is 3.14×10^{-16} m^3 Pa^{-1}, which accounts for 6.6% of the B_d used in our measurements (4.75×10^{-15} m^3 Pa^{-1}, corresponding to zero "additional volume"). Therefore, such a problem is not severe in our system. In addition, the uncertainty analyses following the method given by Ref. 29 also testify to a high confidence level of the permeability and S_s-I data that was obtained using the PPO method.

Secondly, following the poroelastic theory introduced by Brace et al.,[5] the specific storage could be calculated as a function of the porosity, bulk, fluid, and mineral compressibility (β_b, β_f and β_m) as follows:

$$S_s = \beta_b + \Phi\beta_f - (1 + \Phi)\beta_m \tag{2}$$

Following Zimmerman,[32] bulk compressibility can be determined

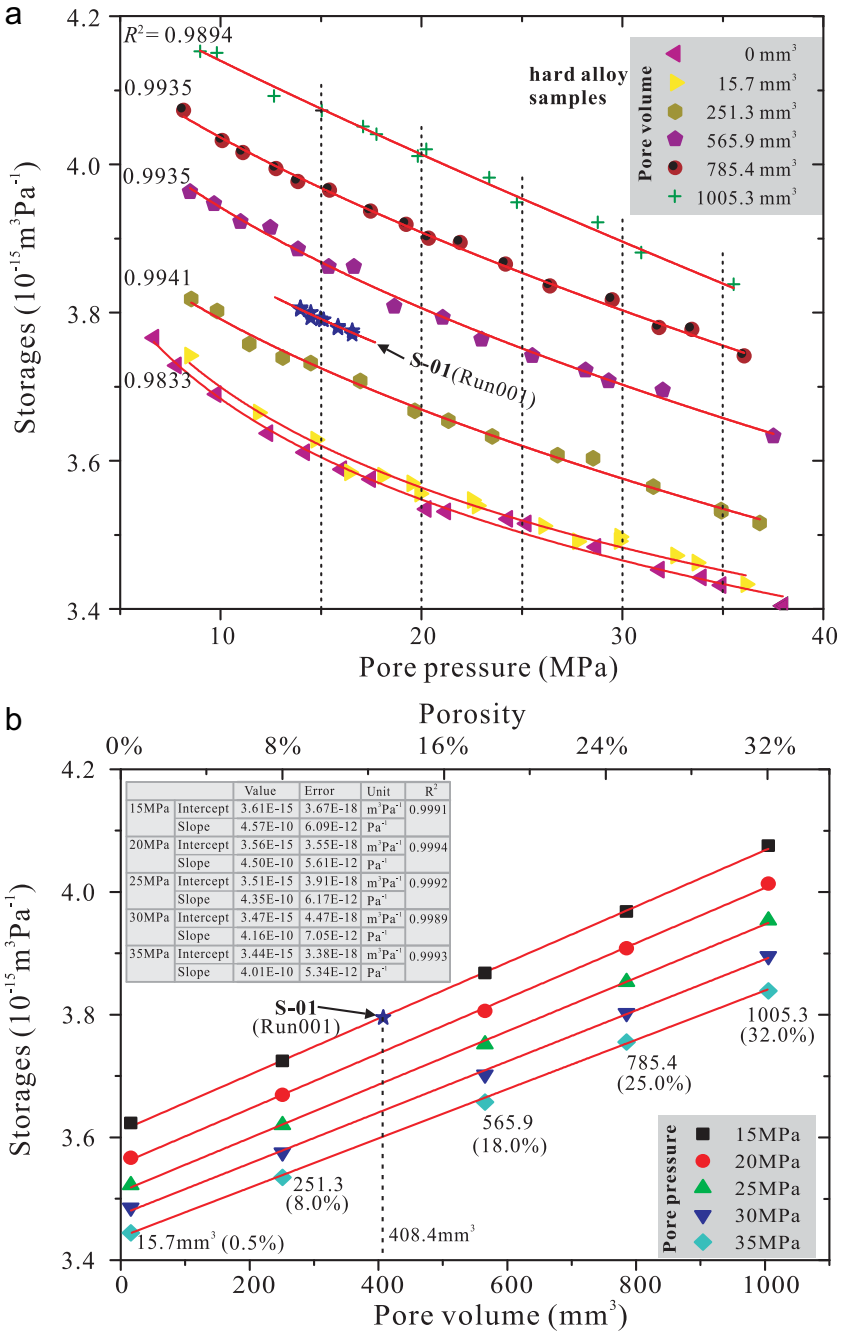

		Value	Error	Unit	R^2
15MPa	Intercept	3.61E-15	3.67E-18	m^3Pa^{-1}	0.9991
	Slope	4.57E-10	6.09E-12	Pa^{-1}	
20MPa	Intercept	3.56E-15	3.55E-18	m^3Pa^{-1}	0.9994
	Slope	4.50E-10	5.61E-12	Pa^{-1}	
25MPa	Intercept	3.51E-15	3.91E-18	m^3Pa^{-1}	0.9992
	Slope	4.35E-10	6.17E-12	Pa^{-1}	
30MPa	Intercept	3.47E-15	4.47E-18	m^3Pa^{-1}	0.9989
	Slope	4.16E-10	7.05E-12	Pa^{-1}	
35MPa	Intercept	3.44E-15	3.38E-18	m^3Pa^{-1}	0.9993
	Slope	4.01E-10	5.34E-12	Pa^{-1}	

Fig. 3. Calibration data of absolute porosity measurement using water as pore fluid. (a) Measured storage as a function of the pore pressure for hard-alloy samples with varied "pore space"; (b) Measured storage as a function of the pore volume at representative fluid pressures.

Table 1
Testing samples and related information.

Sample Unit	Lithology	Length mm	Diameter mm	Mineral composition	Grain density g/cm³	Grain comp Pa^{-1}	Run
S-01	Steel with hole	10.00	20.00	–	–	–	Run001
Ps-01	Porous steel	10.00	20.02	–	–	–	Run073
Ps-02	Porous steel	10.00	20.04	–	–	–	Run074
A-01	Porous ceramic	17.25	19.43	Q-34%, An-60%, Glass-6%	2.62	1.38×10^{-11}	Run075, Run137
S005-2	Quartz sandstone	9.78	20.49	Q-91%, Fel-6%, Clay-3%	2.53	1.75×10^{-11}	Run076
Zj05	Fault gouge	15.89	19.66	Q-29%, Do-27%, Ca-7%, Fel-2%, Clay-35%	2.47	1.75×10^{-11}	Run004

Notation for the minerals: Q represents quartz; Fel, feldspar; Ca, calcite; Do, dolomite; An, andalusite. The mean grain compressibility is weighted from the compressibility of the constituent minerals. Compressibility of quartz and glass is 1.8×10^{-11} Pa^{-1}; calcite and dolomite, 2.3×10^{-11} Pa^{-1}; feldspar, 1.4×10^{-11} Pa^{-1}; andalusite, 1.1×10^{-11} Pa^{-1}; clay (mica), 1.2×10^{-11} Pa^{-1}(data from Ref. 30).

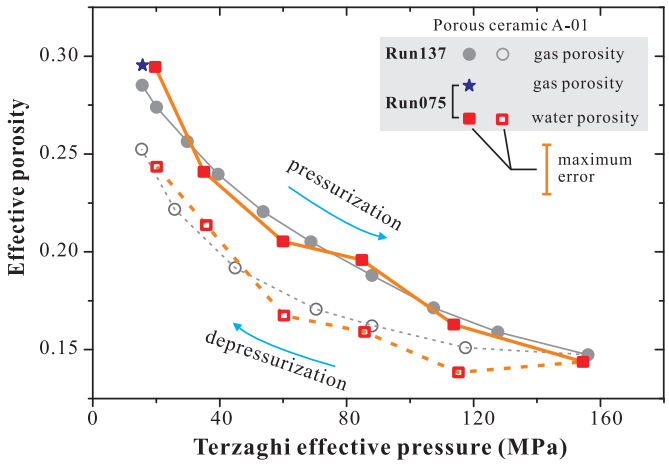

Fig. 4. Effective porosity of a porous ceramic sample under a P_e cycle, using water as pore fluid. Gas porosities of the sample obtained by the gas expansion method were added for comparison.

as $\beta_b = -\frac{1}{V_b}\frac{\partial V_b}{\partial P_c}|_{p=0} = -\frac{1}{V_b}\frac{\partial V_p}{\partial P_c}|_{p=0} - \frac{1}{V_b}\frac{\partial V_m}{\partial P_c}|_{p=0} = -\frac{1}{V_b}\frac{\partial V_p}{\partial P_c}|_{p=0} + (1-\Phi)\beta_m$. This substituted in Eq. (2) becomes

$$S_s = -\frac{1}{V_b}\frac{\partial V_p}{\partial P_c}|_{p=0} + \Phi\beta_f - 2\Phi\beta_m \tag{3}$$

To determine specific storage from Eq. (3), the first term on the right side can be calculated by finding the pore volume change (ΔV_p) per unit of the effective pressure (P_e) change, and dividing it by the sample volume at the start of each step. Published water compressibility (β_f) data, measured porosity (Φ), and grain compressibility (β_m) calculated from compressibility of the constituent minerals and their content (Table 1) are used. The specific storage calculated from Eq. (3) is an "averaged" value over the P_e range of the step,[33] and is hereafter termed as S_s-II. Note that for rock types that have large compressibility, such as the fault gouge, β_m is negligible in comparison to that of the bulk sample, Eq. (3) can be simplified as $S_s = -\frac{1}{V_b}\frac{\partial V_b}{\partial P_c}|_{p=0} + \Phi\beta_f$, which is consistent with those given in previous studies.[8,31]

2.2. Experimental procedure

All samples used were cored to a cylindrical shape. All specimens were 5–40 mm long and approximately 20 mm in diameter. In a typical measurement, a rubber-tube jacked sample is inserted inside the pressure vessel, then connected to the upstream and downstream reservoirs, and loaded to a low confining pressure condition (2 MPa for example). This is followed by evacuating the fluid flow system, and charging it with distilled H_2O. Supposing an initial Terzaghi effective pressure[33,34] ($P_e = P_c - P_f$) of 10 MPa and an average fluid pressure of 15 MPa, the procedure adopted is as follows:

(1) Synchronously increase the confining pressure (P_c) to 25 MPa and fluid pressure (P_f) to 15 MPa, with P_e being kept less than 10 MPa at all times.
(2) After reaching temperature equilibrium (with fluctuations less than 0.1 K), measure the initial (reference) porosity using the microvolumeter, and repeat the measurement for at least three times.
(3) Measure the permeability and specific storage (S_s-I) using the PPO method, or the permeability using the steady-state flow method.
(4) Change the P_c and determine the resultant porosity change.
(5) Repeat steps 3 and 4 at each step change of P_c.

In this way, a set of data, including the permeability, effective porosity, and specific storage (S_s-I and S_s-II), could be obtained for a complete P_c cycle for each sample. Empirically, small P_c steps in size of 5–10 MPa were used for lower pressures ($P_e < 50$ MPa), and large steps of 15–30 MPa for higher pressures ($P_e > 50$ MPa). It should be noted that at any P_c step, the absolute porosity could be checked using the microvolumeter.

3. Results of representative samples

Both natural and analogous rock samples were used for the verification of this study's technique for absolute porosity measurement (Table 1). A stainless-steel cylinder with a hole was first used. As indicated by the stars in Fig. 3a, by adjusting the microvolumeter to varied displacements, we obtained a serious of storages at fluid pressure of around 15 MPa, from which the storage at 15 MPa can be interpolated. According to the 15 MPa calibration curve (Fig. 3b), a pore volume of 408.4 mm^3 can be thus obtained, consistent with the "hole" volume of the sample (408.2 mm^3).

Two commercial porous steel cylinders with standard porosities were also used (Table 1), which, as determined by the gas expansion method (see details in Ref. 8), were $19.7 \pm 0.2\%$ and $18.2 \pm 0.2\%$ at P_e of 35 MPa, respectively. Using water as the pore fluid, the average porosities measured at the same P_e were $20.6 \pm 1.2\%$ and $17.8 \pm 1.4\%$. All of these quantities were consistent with those provided by the company (20.1% and 18.0%).

Then, a porous ceramic sample (Table 1) was further used to examine the sensitivity of the absolute porosity measured to the change in P_e. As shown in Fig. 4, the curve of the porosity obtained showed a rapid reduction as the P_e increased to 60 MPa, followed by a slight decrease afterwards. Meanwhile, along the depressurization path, gentle curves were displayed. These trends were consistent with previous results measured on rock samples using gas as the pore fluid.[2] Moreover, the absolute porosities measured also agreed with that obtained by the gas expansion method (Fig. 4).

Lastly, typical integrated measurement results, i.e. permeability, effective porosity, and specific storages (S_s-I and S_s-II) of a quartz sandstone and a fault gouge under a complete pressure cycle, are presented to show the capabilities of this study's measuring system (Fig. 5). The sandstone represents relatively high-permeability cohesive rock, and the gouge sample represents impermeable incohesive rock. The dimension, composition, grain density and compressibility of these two samples are given in Table 1. All of the permeabilities were measured using the PPO method (Fig. 5a and b). For the effective porosity, we followed the standard procedure, measuring the initial absolute porosity (the red squares with error bars, Fig. 5c and d), and then the porosity change in each P_c step (circles, Fig. 5c and d). For comparison, an absolute porosity measurement was performed on the sandstone at a high pressure ($P_e = 85$ MPa) (Fig. 5c).

As shown in Fig. 5, the solid and open symbols connected with solid and dashed lines denote the data from the pressurization and depressurization paths, respectively. The permeability and the effective porosity curves show a rapid decrease with increasing Terzaghi effective pressure. However, along the depressurization path, they show much gentler trends (Fig. 5a–d). As indicated by the shaded areas (with light and dark shaded areas representing the pressurization and depressurization paths, respectively), the uncertainties to the permeability were small for the range measured ($1 \times 10^{-21}\ m^2 < k < 1 \times 10^{-17}\ m^2$) (Fig. 5a and b). It should be noted that as permeability grew higher ($> 1 \times 10^{-17}\ m^2$) or lower ($< 1 \times 10^{-21}\ m^2$), the phase shift (θ) or amplitude ratio (α) became smaller. The increasing errors in these two parameters

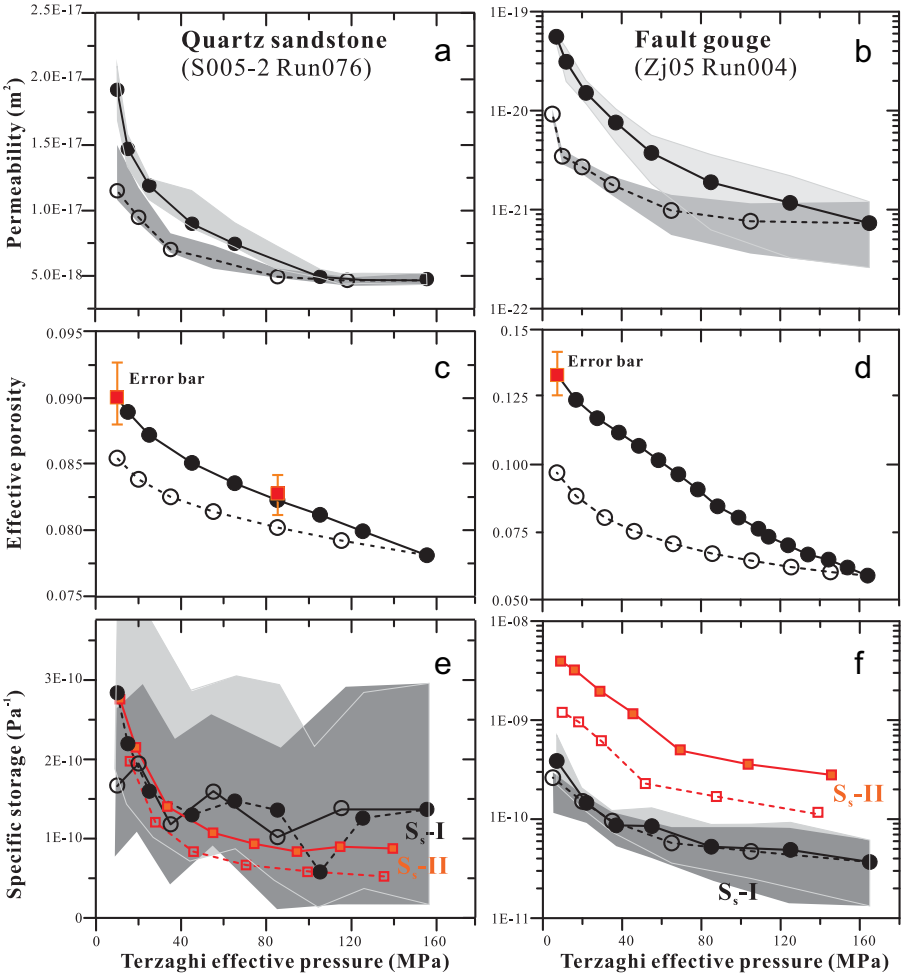

Fig. 5. Integrated measurements of the permeability, effective porosity, and specific storage of a quartz sandstone and a fault gouge, under a cycle of effective pressure up to approximately 160 MPa.

caused a larger uncertainty in the measured permeability. The effective porosity data obtained using the standard procedure exhibits smooth changes along the pressurization and depressurization paths (Fig. 5c and d). For the sandstone, the effective porosity measured at P_e of 85 MPa using the standard procedure agrees with that obtained from the absolute measurement (Fig. 5c). The S_s-II data showed separated curves for the pressurization and depressurization paths, the former having larger values (Fig. 5e and f), presumably due to the fact that the bulk compressibility (β_b) of the sample was smaller along the depressurization path.[33] For the sandstone, the S_s-I and S_s-II were approximately at the same level (Fig. 5e), while for the fault gouge sample, the S_s-I were lower than S_s-II by a factor of one magnitude (Fig. 5f). This discrepancy was inferred from the high bulk compressibility of the gouge sample. When the confining pressure was stepped upward (typically by 10–20 MPa), then a strong compaction should have occurred to gouge sample, accounting for high bulk compressibility, which, however, cannot be measured in the PPO tests, where the fluid pressure was oscillated in a small amplitude (<1 MPa) so that only the elastic strain occurred.[8] On the contrary, for the sandstone, the bulk compressibility was relatively small.

4. Discussion

One of the advantages of the method reported in this study is that the measurement of the absolute porosity utilizing water as pore fluid. When compared with previous measurement results where gas was used as pore fluid, the water porosity is able to reflect the fluid capacity of porous rocks under in-situ hydrological conditions. A second advantage of our method is the concurrent measurement of various transport properties. Despite the improved measuring efficiency, this is essentially important when the sample measured is precious. An integrated measurement is also helpful for deriving the inter-relationships of different parameters, for example: k–Φ,[17] because the influences from the rock's inhomogeneity can be significantly eliminated. Another advantage is that the fluid-flow system enables versatile ways to determine the transport parameters. In the case of permeability for instance, in addition to the steady-state flow and PPO methods addressed above, the pulse-decay method can also be applied. As shown in Fig. 2b, in response to a pressure "pulse" imposed by the microvolumeter, the upstream and downstream pressures exhibit transient changes towards equilibrium, from which the permeability can be calculated. Finally, the experimental procedure proposed in this study is relatively fast. For example, it typically requires one hour to complete a three-parameter measurement at one P_c step for samples with a permeability of $\sim 10^{-21}$ m^2.

The greatest challenge of this method also lies in the measurement of porosity. For the absolute measurement, the uncertainties mainly originate from the fluctuations in environmental temperatures,[21,22,35] which cause errors in determining the pressure change (Δp) generated by the microvolumeter. Our setup has almost no additional void space and even small changes in

ambient temperature induced pressure responses. Therefore, our measurements were performed only if the amplitude of temperature changes was less than 0.1 K during individual measurements. When evaluated as $\Delta T\Lambda$, where ΔT is the temperature fluctuation, and Λ is the thermal pressurization coefficient of the system (0.21 MPa K^{-1}), a temperature fluctuation of 0.1 K will cause an uncertainty in Δp of approximately 1% (assuming a typical Δp of 2 MPa). Performing conventional error propagation analysis, this will cause a standard error in V_p of 78 mm^3, and in porosity of 2.5% for a typical core sample in size of $\varphi 20 \times 10$ mm^2. The temperature variation recorded was then used to determine the uncertainty of the absolute porosity measured. As seen in Figs. 4 and 5, this error is not severe for the samples measured in the present study. However, for low porosity samples ($<5\%$), a temperature fluctuation of 0.1 K can produce a relative error as large as 40%. In cases such as this, the measurements need to be done in an environment with better temperature control in the future. Another means suggested in this study for reducing the uncertainty of absolute porosity is repetitive measurements (see the S-01 sample in Fig. 3a).

The factors influencing the accuracy of porosity change measurements include: (1) the precision of the pressure transducers (E_P); (2) the fluctuations of the environmental temperature (E_T); and (3) the error in calculating grain deformation (E_G). The E_P is expressed as $E_P=\delta PB^*$, where B^* is around 4×10^{-15} m^3 Pa^{-1} for typical samples measured (Fig. 3) and δP is the relative tolerance of the pressure transducer used (0.02 MPa). E_T can be written as $E_T=\Delta T\Lambda B^*$. Substituting the values gives an E_P of 0.08 mm^3, and an E_T of 0.082 mm^3 (assuming a temperature fluctuation of 0.1 K). Supposing an error in grain compressibility to be 1.0×10^{-11} Pa^{-1}, and a typical P_c change of 20 MPa, then the uncertainty in volumetric strain caused by mineral deformation is 2.0×10^{-4}. For a typical sample in size of $\varphi 20 \times 10$ mm^2, this corresponds to an error in volume change of 0.63 mm^3 (E_G). All of these uncertainties, for example, E_P, E_T, and E_G, are relatively small compared with the typical pore volume change measured (10–35 mm^3) for samples of such size. However, it should be kept in mind that the pore volume at each P_c was calculated iteratively from the last step, and the uncertainties were also accumulated. In addition to these effects, previous studies revealed that the jackets can influence the porosity measurement as it can deform into the pores at the surface of the sample when confining pressure is increased.[21] However, we believe the jacket effect was negligible in this study because the verification tests indicated that the jackets used can deform into the void space at P_c as low as 1.5 MPa.

Moreover, our measurements showed a hysteresis effect in all of the three parameters measured (Figs. 4 and 5). In general, the pressurization path leads to higher values than the depressurization path. These pressure cycling tests thus demonstrate that the reported transport properties of the samples, such as those in Fig. 5, depend on the stress history. An important question to address is how the laboratory measurements of transport properties are related to in situ geological conditions. Take fault zone porosity for instance. If fault-zone pore pressure is elevated by a process such as frictional heating, the porosity measured along the pressurization path is representative of the initial porosity at depth, while the porosity evolution of the sample that is recovered from the in-situ depth to lower effective pressures is responsible for the pore fluid pressurization process. Therefore, the application of the measured properties to natural conditions strongly depends on the geological scenario that is involved, and needs to be treated with caution.

5. Concluding remarks

In this study, by using a newly developed microvolumeter, absolute porosity of porous rocks can be measured under an intravessel condition with water as pore fluid. Using the PPO method, the permeability and specific storage could be simultaneously determined. Specific storage can also be calculated by utilizing the poroelastic theory proposed by Brace et al.[5]. By sequentially arranging these methods, a measuring procedure allowing for the integrated measurements of permeability, effective porosity, and specific storage of core samples in a complete pressure cycle was developed.

Acknowledgment

This study was supported by the Basic Scientific Funding of Chinese National Nonprofit Institutes (IGCEA1405), the NSF of China (No. 41372202 and No. 41102130). We thank the anonymous reviewer for their constructive comments, which greatly improved this manuscript.

References

1 Freeman DL, Bush DC. Low-permeability laboratory measurements by non steady-state and conventional methods. *Soc Petrol Eng J.* 1983;23:928–936.
2 Tanikawa W, Shimamoto T. Klinkenberg effect for gas permeability and its comparison to water permeability for porous sedimentary rocks. *Hydrol Earth System Sci Disc.* 2006;3:1315–1338.
3 Haskett SE, Narahara GM, Holditch SA. A method for simultaneous determination of permeability and porosity in low-permeability cores. *SPE Formation Eval.* 1998;3:651–658.
4 Abdulraheem A, Mohiuddin MA, Korvin G, et al. Parametric study of ultrasonic velocity using reservoir cores for enhancing seismic signatures for improved reservoir definition. *1999 SPE Technical Symposium*, Dhahran, Saudi Arabia; 1999:111–120.
5 Brace WF, Walsh JB, Frangos WT. Permeability of granite under high pressure. *J Geophys Res.* 1968;73:2225–2236.
6 Fischer GJ, Paterson MS. Measurement of permeability and storage capacity in rocks during deformation at high temperature and pressure. In: Evans B, Wong T-F, editors. *Fault mechanics and transport properties of rocks.* New York: Academic Press; 1992. p. 187–211.
7 Scheidegger AE. *The physics of flow through porous media.* 3rd ed.,Toronto: University of Toronto Press; 1974.
8 Chen J, Yang X, Duan Q, Shimamoto T, Spiers CJ. Importance of thermochemical pressurization in the dynamic weakening of Longmenshan fault during the 2008 Wenchuan earthquake: inference from experiments and modeling. *J Geophys Res.* 2013;118:4145–4169.
9 Tanikawa W, Shimamoto T. Comparison of Klinkenberg-corrected gas permeability and water permeability in sedimentary rocks. *Int J Rock Mech Min Sci.* 2009;46:229–238.
10 Jones FO, Owens WW. A laboratory study of low-permeability gas sands. *J Pet Technol.* 1980:1631–1640.
11 Faulkner DR, Rutter EH. Comparisons of water and argon permeability in natural clay-bearing fault gouge under high pressure at 20 °C. *J Geophys Res.* 2000;105:16415–16426.
12 Behnsen J, Faulkner DR. Water and argon permeability of phyllosilicate powders under medium to high pressure. *J Geophys Res.* 2011;116:B12203.
13 Duan Q, Yang XS. Experimental studies on gas and water permeability of fault rocks from the rupture of the 2008 Wenchuan earthquake, China. *Sci China Earth Sci.* 2014;57(11)2825–2834.
14 Kwon O, Herbert BE, Kronenberg AK. Permeability of illite-bearing shale: 2. Influence of fluid chemistry on flow and functionally connected pores. *J Geophys Res.* 2004;109:B10206.
15 Xiao X, Evans B, Bernabé Y. Permeability evolution during non-linear viscous creep of calcite rocks. *Pure Appl Geophys.* 2006;163:2071–2102.
16 Milsch H, Spangenberg E, Kulenkampff J, Meyhöfer S. A new apparatus for long-term petrophysical investigations on geothermal reservoir rocks at simulated in-situ conditions. *Transp Porous Media.* 2008;74:73–85.
17 Crawford BR, Faulkner DR, Rutter EH. Strength, porosity, and permeability development during hydrostatic and shear loading of synthetic quartz-clay fault gouge. *J Geophys Res.* 2008;113:B03207http://dx.doi.org/10.1029/2006JB004634.
18 Blöcher G, Zimmermann G, Milsch H. Impact of poroelastic response of sandstones on geothermal power production. *Pure Appl Geophys.* 2009;166(5–7) 1107–1123.
19 Morrow CA, Lockner DA. Permeability and porosity of the Illinois UPH 3 drillhole granite and a comparison with other deep drillhold rocks. *J Geophys Res.* 1997;102:3067–3075.
20 Milsch H, Blöcher G. Direct and simultaneous measurements of sandstone porosity, permeability, and electrical conductivity at elevated pressures. *In: Poromechanics V*; 2013:1415–1424.

21 Blöcher G, Reinsch T, Hassanzadegan A, Milsch H, Zimmermann G. Direct and indirect laboratory measurements of poroelastic properties of two consolidated sandstones. *Int J Rock Mech Min Sci.* 2014;67:191–201.
22 Hassanzadegan A, Zimmermann G. A poroelastic description of permeability evolution. *Pure Appl Geophys.* 2013;171(7)1187–1201.
23 Hassanzadegan A, Blöcher G, Milsch H, Urpi L, Zimmermann G. The effects of temperature and pressure on the porosity evolution of Flechtinger Sandstone. *Rock Mech Rock Eng.* 2014;47(2)421–434.
24 Rutter E, Maddock R, Hall S, White S. Comparative microstructures of natural and experimentally produced clay-bearing fault gouges. *Pure Appl Geophys.* 1986;124:3–30.
25 Huang WL, Longo JM, Pevear DR. An experimentally derived kinetic model for smectite-to-illite conversion and its use as a geothermometer. *Clays Clay Minerals.* 1993;41:162–177.
26 Mohan K, Fogler H. Colloidally induced smectitic fines migration: existence of microquakes. *AIChE J.* 1997;45:565–576.
27 Morrow CA, Moore DE, Lockner DA. The effect of mineral bond strength and adsorbed water on fault gouge frictional strength. *Geophys Res Lett.* 2000;27:815–818.
28 Kranz RL, Saltzman JS, Blacic JD. Hydraulic diffusivity measurements on laboratory samples using an oscillating pore pressure method. *Int J Rock Mech Min Sci Geomech Abstr.* 1990;27:345–352.
29 Bernabé Y, Mok U, Evans B. A note on the oscillating flow method for measuring rock permeability. *Int J Rock Mech Min Sci.* 2006;43:311–316.
30 Vaiday SN, Bailey S, Pasternack T, Kennedy GC. Compressibility of fifteen minerals to 45 kilobars. *J Geophys Res.* 1973;78(29)6893–6898.
31 Wibberley CAJ, Shimamoto T. Earthquake slip weakening and asperities explained by thermal pressurization. *Nature.* 2005;436:689–692.
32 Zimmerman RW, Somerton WH, King MS. Compressibility of porous rocks. *J Geophys Res.* 1986;91(B12)12765–12778.
33 Wibberley CAZ. Hydraulic diffusivity of fault gouge zones and implications for thermal pressurization during seismic slip. *Earth Planets Space.* 2002;54:1153–1171.
34 Terzaghi K. The shearing resistance of saturated soils and the angle between the planes of shear. *In: Proceedings of the first international conference on soil mechanics*, Cambridge: Harvard University; 1936;1:54–56.
35 Morrow CA, Lockner DA, Moore DE, Hickman S. Deep permeability of the San Andreas Fault from San Andreas Fault Observatory at Depth (SAFOD) core samples. *J Struct Geol.* 2014;64:99–113.